# Carrier Photogeneration in Metal-Semiconductor Structures Using Thin Films of Rutile-Phase $TiO_2$ Nanoparticles

Joel Molina, Carlos Zuniga, Edmundo Gutierrez,
Electronics Department,
National Institute of Astrophysics, Optics and Electronics
Santa Maria Tonantzintla, Puebla, Mexico
E-mails: jmolina@inaoep.mx, czuniga@inaoep.mx, edmundo@inaoep.mx

Eunice Mendoza, Jose Luis Sanchez, Erick Bandala
Energy and Environment Research Group,
Universidad de las Americas, Puebla
San Andres Cholula, Puebla, Mexico
E-mails: edith.mendozaco@udlap.mx, jluis.sanchez@udlap.mx, erick.bandala@udlap.mx

***Abstract* — In this work, rutile-phase $TiO_2$ nanoparticles (r-$TiO_2$) are embedded within a Spin-On Glass oxide matrix (using a simple, low thermal budget and economic deposition method) and the final $TiO_2$:$SiO_2$ suspension is used as photoactive material in Metal-Semiconductor structures. For this purpose, so-called "*horizontal*" and "*vertical*" structures are fabricated and characterized under I-V-Light conditions. The electronic, physical, chemical and photovoltaic characteristics of the final structures are obtained and correlated when irradiated with ultraviolet-visible (UV-Vis) light sources. I-V-Light characterization of these structures shows a reduction in the total resistance of thin aluminum stripes or reduction in the resistance state of $TiO_2$:$SiO_2$ composed dielectric when irradiated with UV light (compared to dark conditions). Because of the photogenerated carriers, these structures have *photoresistor* or *photocapacitor* features, which are quite useful for solar energy conversion and storage.**

***Keywords-$TiO_2$ nanoparticles; photoresistor; photocapacitor; photogeneration; sol-gel processing; metal-semiconductor.***

## I. INTRODUCTION

Recently, carrier photogeneration during ultraviolet-visible (UV-Vis) irradiation upon rutile $TiO_2$ nanoparticles has been demonstrated by using so-called "horizontal" and "vertical" metal-semiconductor structures based on binary metal oxides [1]. There, direct exposure of $TiO_2$ nanoparticles to light irradiation enables a reduction in the total resistance of thin aluminum stripes or the sudden increase of the gate current of a Metal-Insulator-Metal (MIM) structure by about 4-7 orders of magnitude, thus showing the potential of $TiO_2$ nanoparticles for photovoltaic conversion and even solar energy storage.

It is widely known that $TiO_2$ (whether in *rutile*, *anatase* or *brookite* crystalline phases) posses enough photocatalytic properties than can be used for efficient conversion of solar energy into electric current if proper device architectures are provided. Photogeneration of electron–hole pairs in $TiO_2$ occurs naturally when this material is irradiated under high energy conditions like ultraviolet-visible light sources, and whose energy (in electron-Volts, eV) is well matched to the energy gap of $TiO_2$. After electron–hole photogeneration, an efficient mechanism for separation of these carriers is needed and the simplest way to achieve this is by developing a large enough electric field so that the negative and positive charges are attracted to the positive and negative polarities of the applied voltage, respectively. These very simple mechanisms of photogeneration and carrier separation by electric field are what most solar cells (mostly based in P–N junctions) use for conversion and handling of an electric current whose magnitude is in direct proportion to the energy and density of radiation being absorbed.

On the other hand, the use of $TiO_2$ nanoparticles for energy conversion is quite attractive given its high contact surface area as compared to a dense bulk film of the same material. This is important since, after irradiation with the proper light sources, a larger density of photogenerated carriers are expected in devices using photoactive nanoparticles. These photogenerated carriers could then be used for more efficient energy conversion ad even, simultaneous energy conversion and storage of the carriers in the same device. In this sense, and even though rutile-phase $TiO_2$ is considered a very inefficient material in terms of its photocatalytic activity (ability for carrier photogeneration) [2-3], use and development of this semiconductor material is quite important since the chemical synthesis of $TiO_2$ usually produces rutile phase $TiO_2$ quite easily, with relatively low concentration of impurities and also, economically. On the other hand, the synthesis of anatase-phase $TiO_2$ is more complicated, usually involving complex chemistry and/or doping with some metal or non-metal elements in order to increase its photocatalytic activity when exposed to UV or visible irradiation [4-7].

Additionally, low thermal budget processing of metal-semiconductor structures based on $TiO_2$ nanoparticles is useful in order to increase the lifetime of photogenerated carriers. This way, relatively higher quantum efficiency during photon-electron conversion is expected and therefore, higher densities of photogenerated currents upon light irradiation. In both our horizontal and vertical devices, a low thermal budget has been kept by using a maximum processing temperature of 250°C, which can be even lowered to 100°C in order to evaporate mostly water and some organic solvents off the $TiO_2$:$SiO_2$ suspension and for film densification. This low-thermal budget process makes these devices ideal for fabrication on large-area flexible substrates (like PET or any other polymer) with the potential to decrease their final costs for widespread use.

In this work, we embed rutile-phase $TiO_2$ nanoparticles (r-$TiO_2$) within an organic $SiO_2$ matrix and the final mixture of this dielectric structure is deposited on thin films of evaporated aluminum stripes. The final "horizontal" metal-semiconductor structure is then electrically characterized under dark and light conditions (I-V-light) so that the total resistance of a simple aluminum stripe is measured and compared before and after UV irradiation. Compared to dark conditions, excess carriers are photogenerated within the $TiO_2$ nanoparticles after light exposure and they are directly transferred to both ends of the aluminum stripe after applying a low potential difference. The highest density of photogenerated carriers is obtained when the $TiO_2$:$SiO_2$/Al is irradiated with UV-B light so that the total aluminum resistance is reduced by about 43%. Therefore, this initial device acts like a very simple "*photoresistor*". Additionally, we also fabricate so-called "vertical" metal-semiconductor-metal structures in order to obtain a solar energy conversion device with the intrinsic ability to self-store must of the converted energy in the form of a rechargeable capacitor. This device then acts like a very simple "*photocapacitor*" [8-9]. The *state-of-the-art* regarding these latest structures makes use of complex layered structures going from photo-rechargeable textiles for wearable power supplies [10], up to dye-sensitized solar cells (DSSC) connected in series with Li-ion batteries, metal oxides and/or $TiO_2$ nanotube arrays in order to increase energy conversion efficiency [11-13]. However, because of increasing fabrication complexity and use of a third additional electrode (in order to switch between the functions of energy conversion, storage and output), which consumes extra energy and increase cost of fabrication, a simpler two-electrode device is needed and that requirement is met by our proposed device structures.

This paper is arranged as follows: in Section I, we gave an introduction about the importance of testing simple "horizontal" and "vertical" metal-semiconductor structures, which make use of $TiO_2$ nanoparticles in order to promote energy conversion in "*photoresistor*" and "*photocapacitor*" devices. Section II presents the experimental conditions used for fabrication of these structures as well as details about the measurement setup that is used for their physical and photo-electrical characterization. Section III presents and discusses the main experimental results that are found for these structures, thus confirming the ability of r-$TiO_2$ to act as photoactive material for both conversion and storage of solar energy. Finally, the main conclusions drawn from all results are highlighted in Section IV, from where we state that it is possible to use the "vertical" structure as a *photocapacitor*, thus enabling direct storage of solar energy.

## II. EXPERIMENTAL

### A. Deposition of Thin Metal Films by Electron-Beam Evaporation under Ultra-High Vacuum Conditions

For the horizontal $TiO_2$:$SiO_2$/Al/Glass structures, and previous to depositing $TiO_2$ nanoparticles on Corning glass slides (2947, size of 75 mm × 25 mm), the initial substrates were degreased by ultrasonic cleaning in trichloroethylene and acetone (10 min and 10 min, respectively). After cleaning the Corning glass slides, 400 nm of aluminum was deposited on one surface of the substrates by e-beam evaporation under ultra-high vacuum conditions (UHV). A metal mask was used during this metallization so that relatively large stripes of aluminum (18mm× 3mm) were left on the glass slides and these substrates are now ready for deposition of $TiO_2$:$SiO_2$ suspensions. For the vertical Ti/$TiO_2$:$SiO_2$/Al/Glass structures, 400 nm of aluminum are initially deposited on one surface of the cleaned glass slides without using any metal mask. This initial aluminum layer works as the bottom electrode of the MIM structure. After deposition of the $TiO_2$:$SiO_2$ suspension, 100 Å of titanium is then deposited by e-beam evaporation (also in UHV conditions). This second metallization with titanium is now performed through a metal mask so that stripes (same size as before) are left on top of the final vertical structure. For all aluminum and titanium metallization, a same deposition rate of 1 Å/sec inside a vacuum of $10^{-7}$ Torr was used.

### B. Preparation of Thin FilmsBased on $TiO_2$ nanoparticles Embedded within an Organic $SiO_2$ matrix

We have used a low-organic content or silicate-type spin-on glass (SOG)-based $SiO_2$ (700B from Filmtronics, Corp.) as a matrix for immobilization of r-$TiO_2$ (Dupont, R-706 with 93% purity and having an average diameter of 360 nm before embedding). Initially, specific amounts of commercial r-$TiO_2$ are suspended in deionized water by hydrolyzing this $TiO_2$:$H_2O$ mixture in a hot water bath (*baine marie*, 45°C, 30 min) and then, adding SOG-based $SiO_2$ so that the final $TiO_2$:$SiO_2$:$H_2O$ mixture is again subjected to a final hot water bath (*baine marie*, 80°C, 1 hr) in order to obtain an homogeneous suspension. The concentration ratios of $TiO_2$ (solute) to $SiO_2$:$H_2O$ (solvent) are 200, 100, 50 and 10 mg/mL and these suspensions are labeled as A, B, C and D, respectively. The solute concentrations were measured with an analytical balance AG285 from Mettler-Toledo. The final $TiO_2$:$SiO_2$:$H_2O$ suspensions were directly applied on the surface of glass slides (Corning glass 2947, size of 75 mm X 25mm), that were previously metalized with aluminum stripes. The suspensions were first spinned at 3000 rpm, 30 sec, and then 4000 rpm, 15 sec in order to obtain uniform layers of r-$TiO_2$ embedded in $SiO_2$. After spinning, all films (A-D) were baked for 2 hours using a hot plate at 250°C in $N_2$ flow (99.99% purity) in order to evaporate mostly water and some of the organic solvents present in the SOG-based $SiO_2$ matrix. For FTIR characterization, the same processing sequence was followed and the final solution was applied on prime-grade P-type silicon wafers (100) with resistivity of 5–10 Ω·cm in order to eliminate most of the organic and impurity elements present within the Corning glass slides. Given the ultra low thermal budget required for fabrication of these simple structures, their introduction into large area flexible substrates is expected, thus promoting wide spread use of optimized devices. The fabrication process flow for both structures is briefly summarized in Figure 1.

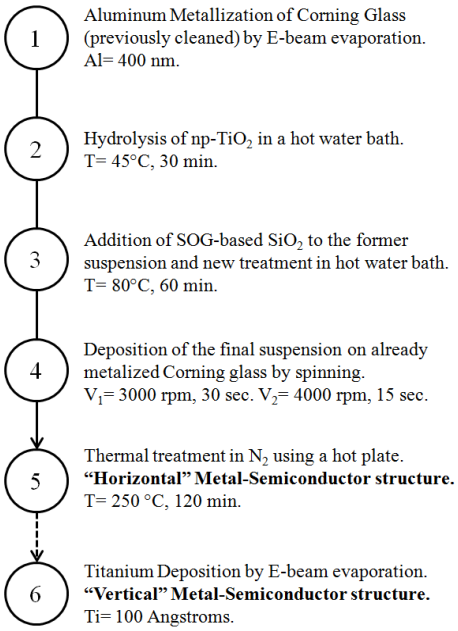


Figure 1. Process flow for fabrication of "horizontal" and "vertical" Metal-Semiconductor structures using r-$TiO_2$ as photoactive material.

It is important to notice that we did not synthesize the r-$TiO_2$ used for fabrication of all proposed structures. Instead, we decided to use readily available commercial $TiO_2$ nanoparticles (with rather low purity of 93% and large average diameter of 360 nm) in order to test the ability of this material for carrier photogeneration under several sources of light irradiation.

### C. *Chemical and Physical Characterization of $TiO_2$ nanoparticles Embedded within $SiO_2$*

Dynamic-Light Scattering (DLS) measurements (Nanotrac Wave, from Microtrac) [14] were done in order to determine the final size distribution of $TiO_2$ nanoparticles after the embedding process. By using DLS, we are able to determine both the size and size distribution profile of $TiO_2$ nanoparticles in the final suspension (before deposition on metalized glass surfaces). In particular, the size distribution profile for r-$TiO_2$ is obtained with high accuracy by this system (close to 100% signal intensity), thus giving a direct estimation of the homogeneity of the r-$TiO_2$ in the final suspension. Also, thicknesses for all films were measured by profilometry (DEKTAK, V200-SI) after partially etching the $TiO_2$:$SiO_2$ film using a strong acid solution composed of diluted HF (HF:$H_2O$, with 1:2 ratio). The crystalline phases of the resulting $TiO_2$-based films were obtained after XRD measurements using an X-ray diffractometer (Empyrean, from PANalytical), with a scanning step of 0.02°, using Cu-$K_\alpha$ radiation with $\lambda$= 1.5406 Å as an X-ray source. The band gap energies Eg of the resulting films were calculated using optical transmittance data measured with an UV-Vis absorption spectrometer (LAMBDA 3B with double beam from Perkin Elmer, with Corning glass used as substrate) and the Tauc method [15]. Chemical compositional analyses for all films were obtained by FTIR spectrum measurements in absorbance mode with a Bruker Vector-22 system after 5 min of purge in $N_2$. The samples were measured against crystalline silicon substrate or SOG based silicon dioxide on glass (both were used as references).

### D. *Electrical Characterization of Horizontal and Vertical Metal-Semiconductor Structures under I-V-Light*

As stated before, only the most concentrated suspension (A suspension) was used for fabrication of the horizontal and vertical structures and therefore, for I–V–Light characterization (I–V measurements under dark/illumination conditions). For characterizing these final structures we have used an HP4156B semiconductor parameter analyzer at 300 K. As light source, we have used natural light conditions of sunlight coming indirectly to the laboratory room, sunlight plus a white lamp put right above all the structures and an UV-B lamp (~ 300nm). For the horizontal structure, an I–V sweep was applied to the ends of the same aluminum stripe while limiting the current compliance to 100 mA. For the vertical structure, an I–V measurement in sampling mode was used where the gate current was constantly monitored with time while the gate voltage was kept constant at Vg = 10 V. In this latter case, the gate current was limited to 100 μA. For all structures, I-V-Light measurements were applied to at least 10 different metal-semiconductor devices in order to obtain typical experimental data.

## III. RESULTS AND DISCUSSION

### A. *Structure's Schematics and Energy Band Diagrams*

Figure 2 shows the 3-D and top view schematics for the horizontal $TiO_2$:$SiO_2$/Al/Glass structure that has been used as a photoresistor upon irradiation of different light sources.

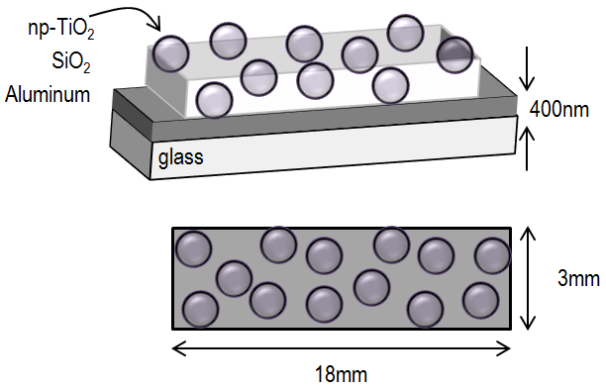


Figure 2. 3D and top views of r-$TiO_2$:$SiO_2$ deposited on Aluminum/Glass.

Because of the preparation method (previously discussed), uniform distribution of the r-$TiO_2$ within the oxide matrix is promoted so that these nanoparticles should have almost the same diameter size and separation in between as well. The aluminum stripes have an area of 18X3 $mm^2$ with thickness of 400 nm. For this structure, I-V-Light characterization takes place by measuring a current flow at

both ends of the same bottom aluminum electrode while both bottom and top electrodes are used in the vertical structure.

Figure 3 shows the idealized energy band diagrams for $TiO_2$ and $TiO_2$:$SiO_2$/Al systems during photogeneration of carriers after irradiation with energies greater than the band gap of $TiO_2$ hν≥Eg($TiO_2$). The band gap Eg, in semiconductor theory, is the void energy region that separates the valence band from the conduction band. For $TiO_2$, the band gap can be overcome with energy from near UV photons. In the first band diagram, all physical mechanisms during light irradiation, (1) excitation, (2) relaxation and (3) diffusion are also shown while a small potential difference is developed in the second diagram so that carriers are injected in the metal. Excitation of a $TiO_2$ system with any light irradiation source having an energy hυ ≥ Eg ($TiO_2$), will generate an electron-hole pair density proportional to the irradiation density of the light source. These photogenerated electron and hole pairs are then enabled for electrical conduction within the conduction and valence bands, respectively. After excitation, relaxation mechanisms lower the potential energy of the excited carriers and then, diffusion by means of a concentration gradient, or even drift, by means of an applied electric field, is possible.

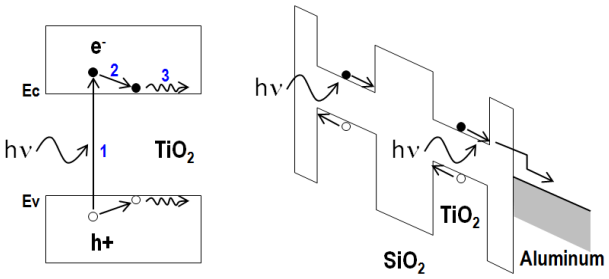


Figure 3. Idealized energy band diagrams for $TiO_2$, $TiO_2$:$SiO_2$/Al systems.

By applying a small potential difference to opposite ends of the same bottom aluminum electrode (see Figure 2 and right side of Figure 3), photogenerated carriers are then injected into this metal and immediately separated by the electric field, thus decreasing its original bulk resistance. In the vertical structure, a potential difference applied to both top/bottom electrodes would separate all photogenerated carriers thus increasing the level of the original gate current (decreasing the original resistance state of the combined $TiO_2$:$SiO_2$). In both cases, we do not take into account most of the physical mechanisms responsible for lowering the quantum efficiency of the structures: trapping, recombination, phonon interaction, annihilation, interface defects, etc. However, those mechanisms and defects are important in order to properly engineer the fabrication process for these structures and then, increase their quantum efficiency for less energetic sources like visible instead of UV irradiation (reducing Eg or increasing the lifetime of photogenerated carriers before recombination).

On the other hand, the photocatalytic properties of $TiO_2$ (quite useful for its bactericide properties) are derived from the formation of photogenerated charge carriers (hole and electron), which occurs upon the absorption of ultraviolet or visible light and that corresponds to the band gap of this material [16-20]. The photogenerated holes in the valence band diffuse to the $TiO_2$ surface and react with adsorbed water molecules, forming hydroxyl radicals ($^{\bullet}OH$). The photogenerated holes and the hydroxyl radicals oxidize nearby organic molecules on the $TiO_2$ surface. Meanwhile, electrons in the conduction band typically participate in reduction processes, which typically react with molecular oxygen in the air to produce superoxide radical anions ($O2^{\bullet-}$). In this sense, because of the high surface contact area presented by $TiO_2$ nanoparticles, this material will generate a large density of electron and hole pairs, which then can be used for both photovoltaic or photocatalytic applications having a high degree of effectiveness.

### *B. Dynamic Light Scattering (DLS) and Profilometry Results for Measuring Diameter of r-$TiO_2$ and Thickness of $TiO_2$ :$SiO_2$ Based Thin Films*

As result of synthesis of the corresponding suspensions, Figure 4 shows the average $TiO_2$ particle diameters for two conditions: as-prepared (measured after at least 24 h of settling time of the synthesized suspensions) and right after sonication using an ultrasonic vibrator (Branson B1510, 2 min at 40 kHz and room temperature). The dotted arrow shows the nominal average diameter as stated by the manufacturer and that is located at about 360 nm. The as-prepared samples present a larger particle diameter because of their tendency to agglomerate or aggregate after dispersion and settling within a liquid suspension. During sonication, enhanced dispersion of $TiO_2$ agglomerates is obtained by overcoming their weaker attractive forces, the final result being smaller $TiO_2$ nanoparticle diameters. The average physical size for sonicated r-$TiO_2$ nanoparticles is around 300 nm. Figure 4 also shows the final $TiO_2$ film's thickness after deposition (by spinning on silicon) and thermal treatment of the prepared suspensions. Thicker $TiO_2$ films were obtained for more concentrated suspensions as expected.

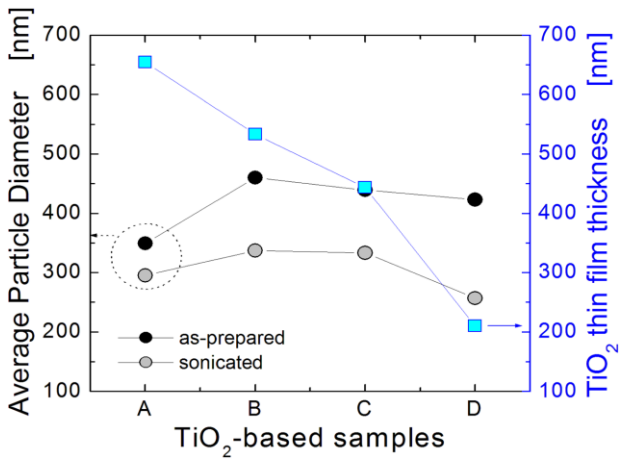


Figure 4. DLS and profilometry data showing the nanoparticle diameter size (before and after sonication) and $TiO_2$:$SiO_2$ thin film thickness, respectively.

As reference, film thickness of SOG based oxide alone (without dilution in $H_2O$) was about 400 nm, which compares well with data obtained for similar spinning conditions [21]. Since all A–D suspensions were prepared using different $TiO_2$:$SiO_2$:$H_2O$ volume ratios (see the experimental procedure), different concentrations of $TiO_2$ within the same matrix would produce different thin film thicknesses. A similar trend of thickness reduction for $SiO_2$ when diluted using different percentages of $H_2O$ was also found by Molina et al. [21] and final thickness of $SiO_2$ could be further reduced when the samples were annealed at higher temperatures. Given that for sample D there is a minimum amount of $TiO_2$ nanoparticles (only 10 mg·mL-1), the final average thickness for this film was kept below the average nanoparticles' diameter because of the reduction in most of the $SiO_2$ thickness by enhanced $H_2O$ dilution and also, because larger amount of water per volume induces further dilution or dispersion of previously agglomerated $TiO_2$ nanoparticles.

Finally, it is important to notice that since these $TiO_2$:$SiO_2$ based films will be under direct irradiation of visible-ultraviolet light sources, measurements of the nanoparticles' sizes and their distribution at both the film's interfaces and in the bulk are necessary to mainly correlate surface distribution of nanoparticles to their carrier photogeneration. These measurements could be done by scanning electron microscopy (SEM) or atomic force microscopy (AFM) for the surface, while transmission electron microscopy (TEM) could be done to obtain the characteristics of the nanoparticles in the bulk of the embedding matrix. These last measurements are actually under progress, and the results will be published elsewhere.

### C. X-Ray Diffraction (XRD)

After obtaining $TiO_2$-based thin films, Figure 5 shows the XRD diffraction patterns for all thin films including sample 0 (only SOG based $SiO_2$), which is only the amorphous matrix of $SiO_2$ deposited atop the glass slides and cured at the same temperature. It is clear that sample 0 does not present the characteristic sharp diffraction peaks of a crystalline material because the incident X-rays are scattered in many directions leading to a large bump distributed over a wide range of 2θ, just like the one shown here for reference purposes. Samples C–D present the lowest intensities for the diffraction peaks related to the crystalline phase of $TiO_2$, since their nanoparticle concentrations were quite small, (50 and 10 mg·mL$^{-1}$, respectively). On the other hand, samples A–B (with concentrations of 200 and 100 mg·mL$^{-1}$, respectively) clearly present the characteristic sharp diffraction peaks for rutile-phase $TiO_2$ including the broad amorphous phase from both the $SiO_2$ matrix and the glass slide (used for $TiO_2$ immobilization and mechanical support purposes, respectively). Given the relatively high concentration density of r-$TiO_2$ embedded within the $SiO_2$ matrix for the A-B samples, it is clear that sharper diffraction peaks will be obtained possibly because of nanoparticles' agglomeration. This effect could be triggered during spinning, which make use of high speed centrifugal forces during step 4 of the process flow; see Figure 1. In particular, sample A showed the clearest and highly intense diffraction peaks, which fit well with those of standard rutile $TiO_2$ (Powder Diffraction File No. 21-1276).

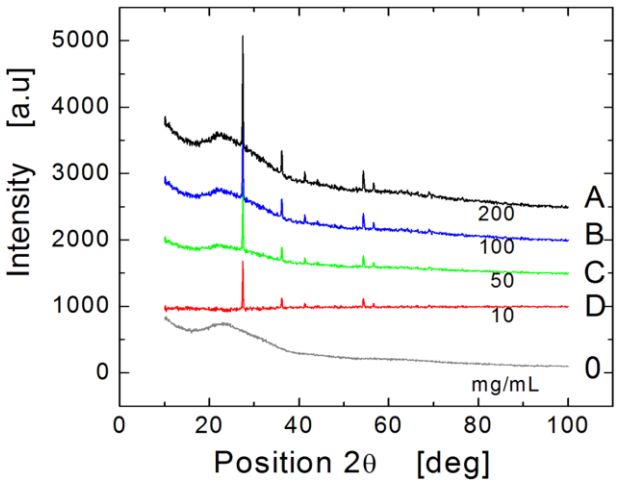


Figure 5. XRD data show existence of rutile phase for $TiO_2$ nanoparticles.

These results provide direct evidence of the existence of rutile phase in the thin $TiO_2$ films after using high $TiO_2$ nanoparticle concentrations (at least 50 mg·mL$^{-1}$). This is important since rutile-phase $TiO_2$ is considered a very inefficient material in terms of its photocatalytic activity and yet, we could obtain moderate photovoltaic activity by using the proposed horizontal and vertical metal-semiconductor structures here discussed.

### D. Fourier-Transformed InfraRed (FTIR) Spectroscopy

The IR spectra for all samples are shown as absorption coefficient a after normalization of each sample to a single and averaged $TiO_2$ film thickness. It is important to notice that these samples are quite different for bulk and dense $TiO_2$ thin films. In these films, the $TiO_2$ nanoparticles tend to disperse within the $SiO_2$ matrix (generating empty spaces) thus avoiding normalization with respect to each physical thickness. Figure 6 shows typical chemical bond vibration energies in absorption mode, found in samples A-D for all the range of interest (wavenumbers from 4000–400 cm$^{-1}$).

The IR spectra for SOG-based $SiO_2$ (deposited on glass) is also included and whose absorption peaks for the Si-O bonds are detected at 1070, 943, 801, 570, and 443 cm$^{-1}$ (peaks 1-5). The bands centered at 1070 and 801 cm$^{-1}$ correspond to symmetric and asymmetric stretching vibrations of Si-O-Si bonds; the bands at 943 and 443 cm$^{-1}$ correspond to bending vibrations of the Si-OH and Si-O-Si bonds, respectively, which confirm that the main composition of this material is $SiO_2$. The absorption band at 570 cm$^{-1}$ is assigned to symmetric Si-O-Si vibrations of the SOG oxide. A decrease in the intensities of the absorption band related to Si-O-Si stretching vibrations was observed for the SOG and D-A spectra (in that sequence), which imply that IR energy is absorbed by the presence of other material.

On the other hand, a combination of both the glass slide and the SOG-based $SiO_2$ present high IR absorption characteristics (high Si–O–Si bond density), which screen-out the presence of any detectable Ti–O–Ti bonds.

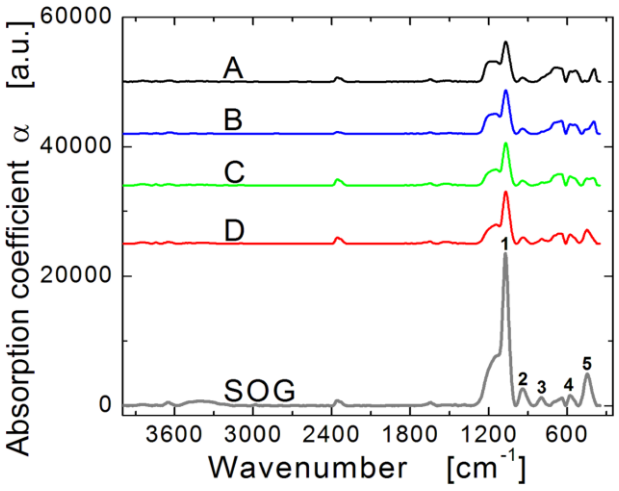


Figure 6. IR spectra (absorbance mode) of $TiO_2$:$SiO_2$/glass samples (A-D). Because of the high density of Si–O and Si–O–Si bonds, the presence of any detectable Ti–O–Ti bonds has been screened out in these measurements.

In order to analyze only the contribution of $TiO_2$ in the films, the IR spectra of A-D samples must be obtained using only the SOG-based oxide film as reference ($SiO_2$/glass) and take these measurements at wavenumber between 1600 and 400 $cm^{-1}$ approximately. This way, we are able to eliminate the influence of the highly absorbent peaks related to Si–O and Si–O–Si bonds (those especially found at 1070 and 443 $cm^{-1}$), which could screen-out the presence of any detectable Ti–O–Ti bonds. Figure 7 shows the new IR spectra (using the $SiO_2$/Glass sample as reference) including some absorption bands at 765 (black arrow at shoulder section), 530 and 395 cm-1.

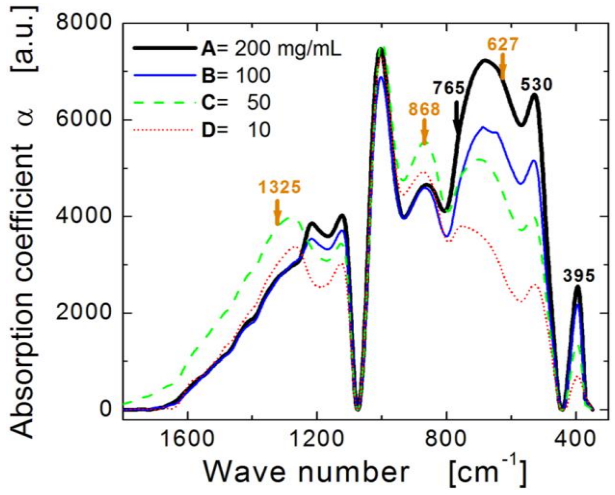


Figure 7. IR spectra (absorbance mode) of $TiO_2$:$SiO_2$/glass samples (A-D) and using $SiO_2$/Glass as reference in order to detect Ti–O–Ti bonds.

The band detected as a shoulder at 765 $cm^{-1}$ is comparable with the IR spectrum of crystalline $TiO_2$ (having anatase or rutile crystalline structure) due to symmetric stretching vibrations of the Ti–O bonds. Most importantly, the absorption peaks for these Ti–O bonds increase with the content of $TiO_2$, thus confirming proper chemical bonding of this photoactive material for even the larger $TiO_2$ concentrations. Also, even though the main absorption bands for the Si–O–Si bonds mostly disappear when SOG-based oxide film is used as reference, some Si–O bonds appear in these samples surely because of vibrations of Si–O–Ti bonds, as observed in the band at 1005 $cm^{-1}$. On the other hand, the bands at 627 and 1325 $cm^{-1}$ are thought to be related to vibrations of some Al–O bonds while the band at 868 $cm^{-1}$ is related to a combination of both Al–O and Si–O bonding vibrations. Detecting contributions of both Al–O and Si–O bonds, make sense considering that commercial $TiO_2$ nanoparticles consist, according to the manufacturer, of 93% $TiO_2$, 2.5% $Al_2O_3$ and 3% $SiO_2$ (the remaining percentage consisting of other undetectable elements).

Figure 8 shows the IR absorption spectra of $TiO_2$:$SiO_2$ films from 4000 to 2600 $cm^{-1}$, where the presence of strong absorption bands in the region of 3200-3500 $cm^{-1}$, (corresponding to bending vibrations of adsorbed and possibly coordinately bounded OH molecules with Ti or Si) are noticed.

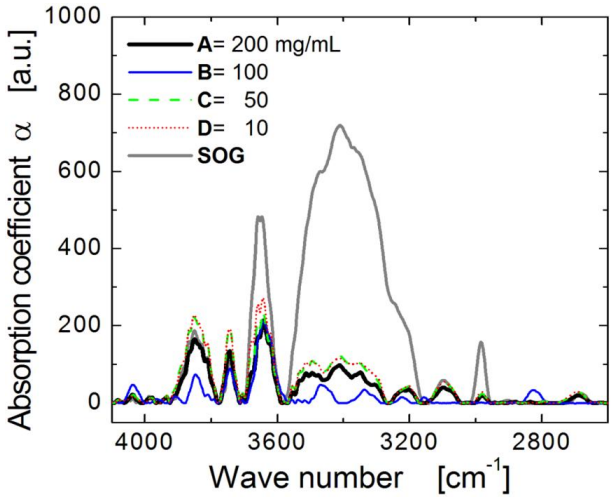


Figure 8. IR spectra (absorbance mode) of $TiO_2$:$SiO_2$/glass samples (A-D) for wavenumbers in the 4000 to 2600 $cm^{-1}$ region. This measurement enables detection of any remaining organic impurities in the samples.

Also, the weak absorption peaks in the region of 2920-2930 $cm^{-1}$ among others are related to the presence of organic residues that were not fully evaporated or decomposed during the low-temperature thermal treatments applied to the $TiO_2$ films. For comparison, the IR spectra for SOG-based oxide is also shown so the main absorption bands related to purely organic elements can be easily identified (having the strongest absorption peaks). Since the highest thermal treatment applied to all A-D samples was only 250°C, higher temperatures for this final curing process would evaporate or reduce these organic residuals more

efficiently. However, for practical applications, it is desired to reduce the total thermal budget for this material so that it could be possible to develop coatings of $TiO_2$ (with enough photovoltaic or light response) on plastic or other economic and readily available flexible substrate for large area applications.

### *E. UV-Vis Transmittance Spectroscopy*

Optical band gap Eg, is an important physical parameter in semiconductor materials because it allows knowing the threshold energies to which a material in particular, like $TiO_2$, is "transparent" or able to absorb incident photons and therefore, create electron-hole pairs that could participate in photovoltaic processes. The UV-Vis spectra from 190 to 900 nm region for the different $TiO_2$ concentrations (A-D samples), including the spectrum for only the glass substrate, are all shown in Figure 9.

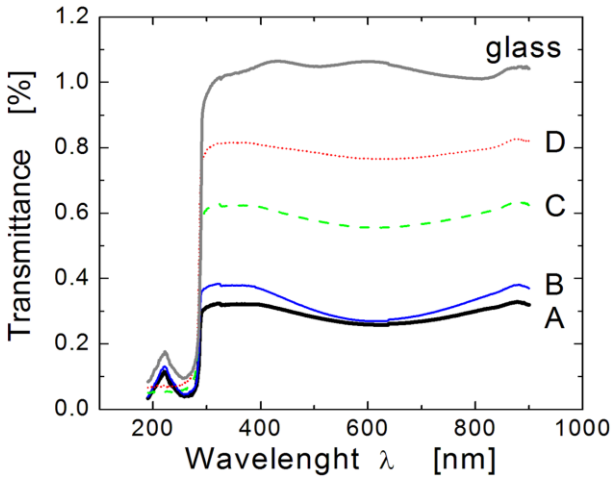


Figure 9. UV-Vis spectra obtained for all $TiO_2$:$SiO_2$ (A–D, Glass) samples showing that transmittance is in reverse proportion to $TiO_2$ concentration.

It can be seen that strong absorption occurs at wavelengths $\lambda$<290 nm (UV-B regime) for all samples and that transmittance is reduced in direct proportion to the r-$TiO_2$ concentration as expected. Even though the physical thicknesses for all samples are different (see Figure 4), minimum variations in their optical band gap are expected if we consider different densities for these films.

Additionally, since the number of interference fringes is not visible, this avoids using the Swanepoel model for optical band gap calculation Eg [22] and therefore, a fast estimation was done to obtain this important parameter. Figure 10 shows the transmittance spectra versus photon energy for the A-D samples. The inflexion point is the crossing for all samples after linearly extrapolating all slopes with the axe for photon energy. The band gap Eg is determined by dividing this inflexion point by $\sqrt{2}$ [23]. The inflexion points cut the photon energy axis at between 4.41–4.42 eV so that the correspondent optical band gap Eg for all A-D samples lies at 3.11-3.12 eV.

This band gap energy Eg corresponds well with the reported Eg for anatase or rutile $TiO_2$, between 3.0 and 3.2 eV, respectively [24-25].

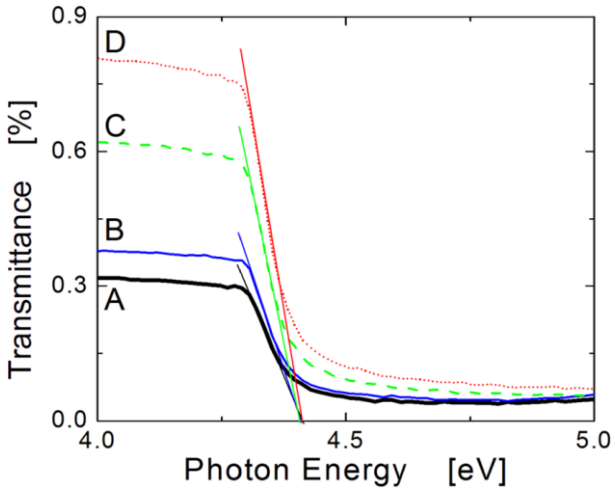


Figure 10. Extrapolation of UV-Vis transmittance data to photon energy for all A-D samples in order to obtain $TiO_2$ band gap energy (Eg).

On the other hand, for the vertical structure (Ti/$TiO_2$:$SiO_2$/Al/Glass device), we make use of an ultra-thin titanium stripe (thickness of 100 Å) in order to use it as a conductive top electrode while being able to transmit most of the UV-Vis irradiation through itself, thus allowing efficient photogeneration of carriers in the $TiO_2$. In order to obtain the optical properties of this electrode, the transmittance spectra (from 190 to 900 nm region) for different ultra-thin titanium films are shown in Figure 11.

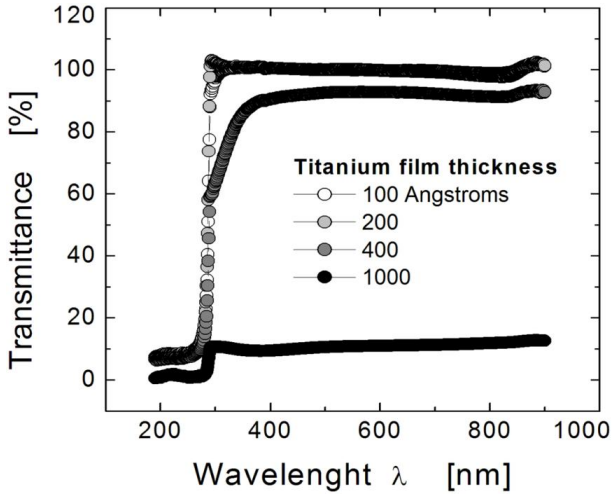


Figure 11. Transmittance (UV-Vis) spectra of ultra-thin titanium films. The titanium film having 100 Å in thickness was used as the top electrode in the vertical Ti/$TiO_2$:$SiO_2$/Al/Glass MIM structures.

We clearly notice that the thinner titanium films (100 and 200 Å in thickness) transmit virtually the complete (100%) electromagnetic spectra from 900 nm down to 290 nm, thus being transparent to the visible, the UV-A and UV-B regions

as well. For the UV-C region, all films readily absorb or reflect this energy so that the transmittance characteristics are lost. For a titanium film of 400 Å in thickness, the original transmittance falls to about 93% from 900 nm down to ~400 nm, thus this sample is transparent to only the visible region of the spectra. At wavelengths of 400 nm and downwards, this sample starts to absorb/reflect UV-A and UV-B thus it is not useful for proper absorption of those energies (by $TiO_2$) in the vertical structures. We also show the very low transmittance characteristics (around 10%) obtained from a thicker titanium film (1000 Å) as a reference.

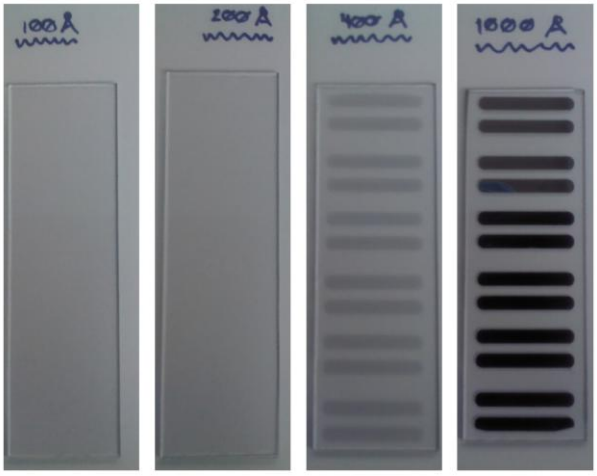


Figure 12. Photograph showing the transmittance quality of ultra-thin titanium films. The titanium films having 100 and 200 Å in thickness (in the form of stripes) are optically transparent while titanium films having 400 and 1000 Å in thickness are opaque since they absorb/reflect most UV.

Figure 12 above shows the optical transparency of thin titanium films deposited on Corning glass slides in the form of stripes (after E-beam evaporation under ultra-high vacuum conditions). We clearly notice that titanium films having 100 and 200 Angstroms in thickness are optically transparent while thicker films are opaque. In our vertical MIM structures, we have used an ultra-thin titanium film (having only 100 Å in thickness) so that we ensure good transmittance characteristics (especially in the UV regime) along with good conductive properties in order to have a transparent-conductive electrode.

### *F. I-V-Light Response of Horizontal $TiO_2$:$SiO_2$/Al/Glass*

Figure 13 shows the I-V-Light characteristics of the structure shown previously in Figure 2 (A sample only). Dark, sunlight, sunlight+lamp and UV-B light (~300 nm) conditions were all applied on top of the structures so that surface r-$TiO_2$ were the first to absorb all possible irradiation coming from these sources. Compared to dark conditions, photogeneration of excess carriers (both electrons and holes) within the $TiO_2$ nanoparticles is greater after UV-B light exposure and these carriers are directly transferred to both ends of the Al-stripe after applying a low potential difference. During UV-B light irradiation, the total aluminum resistance is reduced by about 43%, which represent a moderate change in resistance given by rather low quantum efficiency presented by this structure.

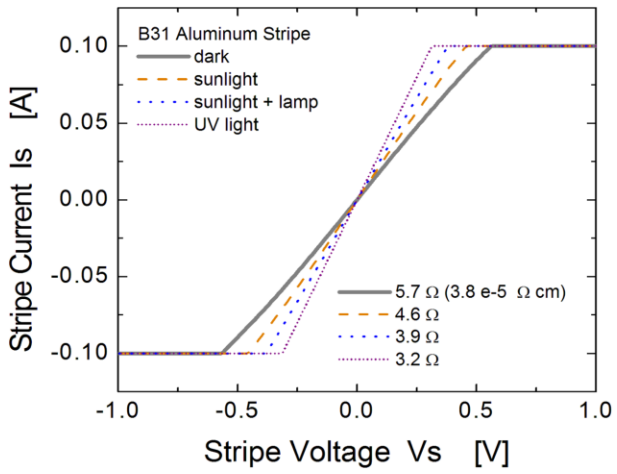


Figure 13. I–V–Light characteristics of an aluminum stripe (horizontal $TiO_2$:$SiO_2$/Al/Glass structure) before and after light irradiation. This device acts as a *photoresistor*.

### *G. I-V-Light Response of Vertical Ti/$TiO_2$:$SiO_2$/Al/Glass*

Previously, I-V-Light characterization for horizontal structures produced a moderate photogeneration of carriers so that the total resistance of an aluminum strip was reduced. However, given that some of the photogenerated carriers will be trapped, recombined or "*lost*" within the $SiO_2$ matrix or at its interface with r-$TiO_2$ (any annihilation mechanism), the "*horizontal path*" followed by carriers in the initial structure would reduce their lifetime once they are photogenerated in the r-$TiO_2$. In order to increase photocarrier lifetime before recombination and thus, increase quantum efficiency during UV-B irradiation, vertical structures are proposed, see Figure 14.

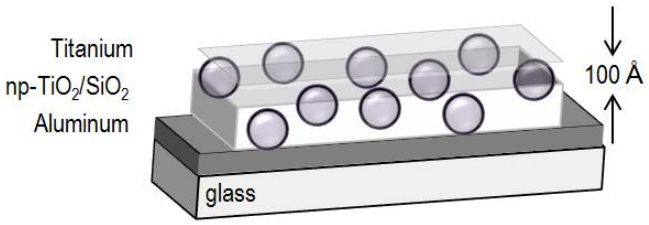


Figure 14. 3D view for a vertical Ti/$TiO_2$:$SiO_2$/Al/Glass structure where the titanium electrode is 100 Å in thickness, thus being optically transparent.

These vertical structures use titanium as a gate electrode (only 100 Å in thickness) so that a capacitor in the form of a Metal-Insulator-Metal structure is formed. Because of the ultra-thin titanium layer, this gate electrode is highly transparent to all UV-Vis irradiation so that when all carriers are being photogenerated, a vertical transition of these carriers between bottom/top electrodes (by an applied external electric field) would require a shorter distance thus

increasing their lifetime before recombination as compared to the horizontal structures.

Figure 15 shows the I–V–Light characteristics (under dark/illumination conditions) of three vertical Ti/$TiO_2$:$SiO_2$/ Al/Glass structures. Here, an I–V measurement in sampling mode (I-time) was used where the gate current Ig was constantly monitored with time and the gate voltage was kept constant (Vg = 10 V, applied at the semitransparent Ti electrode). We notice that the gate current increases about 4-7 orders of magnitude when the structures are exposed to sunlight. A high velocity photo-response to optical excitation is obtained given the shortest vertical transition between top and bottom electrodes.

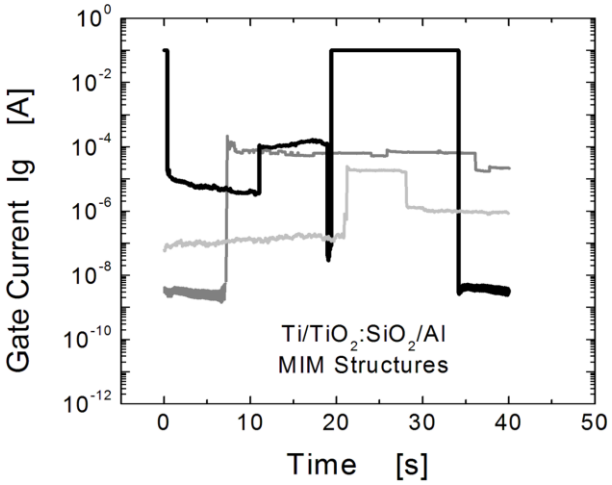


Figure 15. I–V–Light characteristics of three different MIM capacitors (Ti/$TiO_2$:$SiO_2$/Al/Glass structures) before and after sunlight irradiation. All samples present rapid dark-to-illuminated Ig transitions and vice versa. Any of these devices acts as a *photocapacitor*, thus enabling direct storage of solar energy after photogeneration of carriers.

These vertical structures are able to photogenerate and store carriers quite similar to the so-called *photocapacitor* [7-8], where all carriers could be efficiently stored within the dielectric itself right after photogeneration. Thus, a light-driven self-charging capacitor having a direct and efficient storage mechanism of solar energy has been obtained.

## IV. CONCLUSIONS

Photocarrier generation during UV-B exposure of rutile-phase $TiO_2$ nanoparticles in horizontal and vertical metal-semiconductor structures, reduces the total resistance of an aluminum stripe by about 43% or instantly increase the gate current Ig for about 4-7 orders of magnitude, respectively. Both structures can be fabricated using simple and economic processing techniques with low thermal budget. The vertical structure works as a *photocapacitor*, enabling simultaneous conversion and storage of solar energy.

## ACKNOWLEDGMENT

This work was fully supported by the National Council of Science and Technology (CONACyT-Mexico).

## REFERENCES

[1] J. Molina, C. Zuniga, E. Gutierrez, E. Mendoza, J.L. Sanchez, and E.R. Bandala, "Carrier photogeneration during UV-Vis irradiation on horizontal and vertical metal-semiconductor structures based on rutile-phase $TiO_2$ nanoparticles," Proc. of the Fourth International Conference on Sensor Device Technologies and Applications, SENSORDEVICES 2013. vol. 1, pp. 41-45, 2013.

[2] Z. Ding, G.Q. Lu, and P.F Greenfield, "Role of the crystallite phase of $TiO_2$ in heterogeneous photocatalysis for phenol oxidation in water," J. Phys. Chem. B, vol. 104, April 2000, pp. 4815-4820.

[3] T.A. Kandiel, R. Dillert, A. Feldhoff, and D. Bahnemann, "Direct synthesis of photocatalytically active rutile $TiO_2$ nanorods partly decorated with anatase nanoparticles," J. Phys. Chem., vol. 114, February 2010. pp. 4909-4915.

[4] M.A. Behnajady, N. Modirshahla, M. Shokri, and B. Rad, "Enhancement of photocatalytic activity of $TiO_2$ nanoparticles by silver doping: photodeposition versus liquid impregnation methods," Global NEST Journal, vol. 10-1, 2008, pp. 1-7.

[5] D.H. Kim, D.K. Choi, S.J. Kim, and K.S. Lee, "The effect of phase type on photocatalytic activity in transition metal doped $TiO_2$ nanoparticles," Catalysis Communications, vol. 9, March 2008, pp. 654–657.

[6] C.D. Valentin, G. Pacchioni, and A. Selloni, "Origin of the different photoactivity of N-doped anatase and rutile $TiO_2$," Phys. ReV. B., vol. 70, August 2004, pp. 085116-1--085116-4, 2004.

[7] O. Diwald, L. Thompson, E.G. Goralski, S.D. Walck, and J.T. Yates, "The effect of nitrogen ion implantation on the photoactivity of $TiO_2$ rutile single crystals," J. Phys. Chem. B, vol. 108, January 2004, pp. 52-57.

[8] T. Miyasaka and T.N. Murakami, "The photocapacitor: an efficient self-charging capacitor for direct storage of solar energy," Appl. Phys. Lett., vol. 85, October 2004, pp. 3932-3934.

[9] C.W. Lo, C. Li, and H. Jiang, "A photoelectrophysical capacitor with direct solar energy harvesting and storage capability," Optical MEMS and Nanophotonics (OPT MEMS), 2010 International Conference on, August 2010, pp. 65-66.

[10] T. Song and B. Sun, "Towards photo-rechargeable textiles integrating power conversion and energy storage functions: can we kill two birds with one stone?," ChemSusChem, vol. 6, January 2013, pp. 408–410.

[11] X. Zhang, X. Huang, C. Li, and H. Jiang, "Dye-sensitized solar cell with energy storage function through PVDF/ZnO nanocomposite counter electrode," Adv. Mater., June 2013, pp. 1-4.

[12] W. Guo, X. Xue, S. Wang, C. Lin, and Z.L. Wang, "An integrated power pack of dye-sensitized solar cell and Li battery based on double-sided $TiO_2$ nanotube arrays," Nano Lett., vol. 12, no. 5, April 2012, pp. 2520–2523.

[13] M.S. Nuckowska, K. Grzejszczyk, P.J. Kulesza, L. Yang, N. Vlachopoulos, L. Häggman, E. Johansson, and A. Hagfeldt, "Integration of solid-state dye-sensitized solar cell with metal oxide charge storage material into photoelectrochemical capacitor," J. of Power Sources, vol. 234, no. 15, July 2013, pp. 91-99.

[14] "Microtrac: total solutions in particle characterization, NanotracWave," App Note, Microtrac. October 2012, pp. 1-4. http://www.microtrac.com/MTWP/wp-content/uploads/2012/10/Nanotrac-Wave-Temp-Brochure-Ver-9.pdf

[15] J. Tauc, "Optical properties and electronic structure of amorphous Ge and Si," MRS Bulletin, vol. 3, January 1968, pp. 37-46.

[16] A. Fujishima, T.N. Rao, and D.A. Tryk, "Titanium dioxide photocatalysis," J. Photochem. Photobiol. C: Photochem. Rev., vol. 1, March 2000, pp. 1–21.

[17] A. Fujishima, X. Zhang, and D.A. Tryk, "$TiO_2$ photocatalysis and related surface phenomena," Surf. Sci. Rep., vol. 63, December 2008, pp. 515–582.

[18] K. Nakata and A. Fujishima, "$TiO_2$ photocatalysis: design and applications," J. Photochem. Photobiol. C: Photochem. Rev., vol. 13, June 2012, pp. 169–189.

[19] M.R. Hoffmann, S.T. Martin, W. Choi, and D.W. Bahnemann, "Environmental applications of semiconductor photocatalysis," Chem. Rev., vol. 95, January 1995, pp. 69–96.

[20] D.S. Bhatkhande, V.G. Pangarkar, and A.A.C.M. Beenackers, "Photocatalytic degradation for environmental applications – a review," J. Chem. Technol. Biotechnol., vol. 77, January 2002, pp. 102–116.

[21] J. Molina , A.L. Munoz, A. Torres, M. Landa, P. Alarcon, and M. Escobar, "Enhancement of the electrical characteristics of MOS capacitors by reducing the organic content of $H_2O$-diluted spin-on-glass based oxides," Mater. Sci. Eng. B, vol. 176, no. 17, March 2011, pp. 1353-1358.

[22] R. Swanepoel, "Determination of the thickness and optical constants of amorphous silicon," J. Phys. E: Sci. Instrum., vol. 16, no. 12, December 1983, pp. 1214-1222.

[23] M. Sreemany and S. Sen, "A simple spectrophotometric method for determination of the optical constants and band gap energy of multiple layer $TiO_2$ thin films," Materials Chemistry and Physics, vol. 83, no. 1, January 2004, pp. 169–177.

[24] J. Dharma and A. Pisal, "Simple method of measurement the band gap energy value of $TiO_2$ in the powder form using UV/Vis/NIR spectrometer," App Note, Perkin-Elmer Inc. January 2009, pp. 1-4.

[25] S. Valencia, J.M. Marin, and G. Restrepo, "Study of the bandgap of synthesized titanium dioxide nanoparticules using the sol-gel method and a hydrothermal treatment," The Open Materials Science Journal, vol. 4, January 2010, pp. 9-14.